JACS
JOURNAL OF THE AMERICAN CHEMICAL SOCIETY

COMMUNICATION

pubs.acs.org/JACS

Benchtop Electrochemical Liquid–Liquid–Solid Growth of Nanostructured Crystalline Germanium

Azhar I. Carim,[†] Sean M. Collins,[†] Justin M. Foley,[‡] and Stephen Maldonado*[,†,‡]

[†]Department of Chemistry and [‡]Program in Applied Physics, University of Michigan, 930 North University Avenue, Ann Arbor, Michigan 48109-1055, United States

Supporting Information

ABSTRACT: An electrochemical liquid–liquid–solid (ec-LLS) process that produces large amounts of crystalline semiconductors with tunable nanostructured shapes without any physical or chemical templating agent is presented. Electrodeposition of Ge from GeO_2(aq) solutions followed by dissolution into a liquid Hg electrode, saturation of the liquid alloy, and precipitation can yield polycrystalline Ge(s) under ambient conditions. A unique advantage of ec-LLS is that it involves precipitation under electrochemical control, where the applied bias precisely defines the flux of Ge into the liquid electrode. Fidelity of the saturation and precipitation of Ge from liquid electrodes affords a variety of material morphologies, including dense films of oriented nanostructured filaments with large aspect ratios (>10^3). Electrodeposition involving a liquid electrolyte, a liquid electrode, and a solid deposit under ambient conditions represents a conceptually unexplored direct wet-chemical route for the preparation of bulk quantities of crystalline group-IV semiconductors without the time- and energy-intensive processing steps required in traditional preparations of semiconductor materials.

New methods that do not innately require large energy inputs to prepare functional optoelectronic materials from raw sources are crucial for minimizing the environmental impact of the manufacture and processing of group-IV semiconductor-based technologies.[1] No unabated electrodeposition process that produces crystalline rather than amorphous group-IV semiconductors at solid electrodes from oxidized, dissolved precursors has been identified to date. More specifically, strategies for electrodeposition of large amounts of Ge continuously from aqueous solutions in a single step have been previously investigated but proved difficult to develop because of poorly understood self-limiting/surface-fouling processes at solid metal electrodes during Ge electrodeposition.[2−4] Accordingly, we report data demonstrating the use of liquid electrodes as platforms for electrodeposition of *crystalline* Ge directly from aqueous electrolytes without cessation. All potentials reported herein are with respect to a Ag/AgCl (saturated KCl) reference electrode. Without dissolved GeO_2, only a voltammetric response for H_2 evolution was observed at Hg pool electrodes in alkaline solution (Figure 1a). In the presence of 50 mM GeO_2, the cathodic current increased markedly at potentials more negative than −1.2 V at pH 8.5 as a result of reaction 1,

$$HGeO_3^-(aq) + 4e^- + 2H_2O(l) \rightarrow Ge(s) + 5OH^-(aq) \quad (1)$$

indicating that at this formal concentration, the Hg electrode is more electroactive toward reaction 1 than H_2 evolution. The voltammetric response was nominally independent of scan rate, and exchange of the borate buffer with $KHCO_3$(aq) effected no change in the current magnitudes or amount of electrodeposited Ge. Two anodic voltammetric waves were observed at applied potentials (E) of −0.5 and 0.0 V for the oxidation of electrodeposited Ge, as previously described in polarographic reports on electroanalytical Ge detection.[5,6] Chronocoulometric experiments conducted at potentials more negative than −1.2 V on the time scale of hours showed stable and continuous passage of charge for reaction 1 (Figure 1b). A dark, dull particulate film completely coated the electrode interface after polarization at E = −1.9 V for 20 min (Figure S1 in the Supporting Information). By comparison, electrodeposition of Ge onto Cd and Zn, two other group-IIB metal electrodes with similarly poor electrocatalytic properties for H_2 evolution, yielded significantly less Ge (the faradaic efficiencies for Ge electrodeposition at Hg, Cd, and Zn at E = −1.5 V were 89 ± 6, 24 ± 3, and 18 ± 11%, respectively).

The as-collected black film electrodeposited at Hg pool electrodes showed strong evidence of crystallinity. The first-order Raman spectra obtained for Ge electrodeposited at several applied biases exhibited a common, single pronounced signature near 300 cm^{-1}, characteristic of crystalline Ge(s) (Figure 2a).[7] The absence of a mode centered near 270 cm^{-1} indicated no substantial content of amorphous Ge collected at Hg,[8] in contrast to Raman spectra of Ge electrodeposited at Cd and Zn electrodes (Figure S2). The Raman spectra also showed that the potential used for electrodeposition influenced the observed crystallinity. The phonon mode near 300 cm^{-1} was red-shifted slightly and broadened for Ge electrodeposited at increasingly more negative potentials, indicating crystalline domain sizes approaching or below the 24.3 nm Bohr exciton radius for Ge.[9,10] Corresponding FTIR and Raman spectra of these Ge samples bore no detectable evidence of hydrogenation (Figure S3). Separate powder X-ray diffractograms of the electrodeposited Ge (Figure 2b and Figure S4) exhibited reflection patterns consistent with the premise that the as-prepared electrodeposited Ge possessed only a diamond cubic lattice. The relative intensities of the peaks in the diffractograms also indicated no net Ge crystalline orientation at any of the applied potentials. However, the line widths in the diffractograms were sensitive to the electrodeposition potential, with a perceptible broadening of each reflection for Ge electrodeposited

Received: June 14, 2011
Published: August 10, 2011

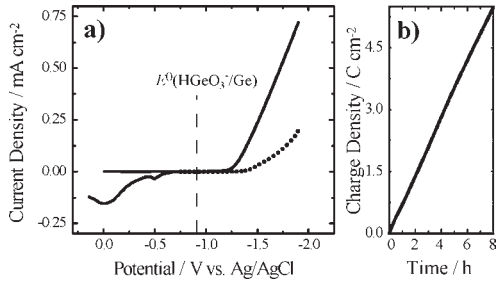

Figure 1. (a) Voltammetric responses for a Hg pool electrode immersed in deaerated 10 mM $Na_2B_4O_7$ (dotted line) without and (solid line) with 50 mM GeO_2 at a scan rate of 0.01 V s^{-1}. The dashed line indicates the standard potential for the $HGeO_3^-$/Ge redox couple at pH 8.5 and 298 K. (b) Chronocoulometric response for a Hg pool electrode immersed in 10 mM $Na_2B_4O_7$ and 50 mM GeO_2 and biased at $E = -1.5$ V vs Ag/AgCl for 8 h.

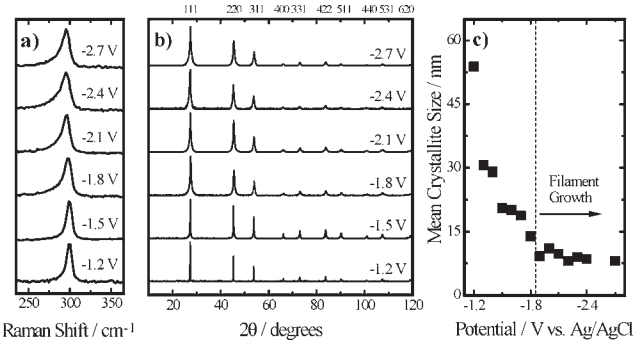

Figure 2. (a) First-order Raman spectra for Ge electrodeposited at a constant potential on Hg pool electrodes immersed in the same electrolyte as in Figure 1 and biased at several discrete potentials with respect to a Ag/AgCl reference electrode. The spectra have been offset for clarity. (b) Powder X-ray diffractograms of Ge electrodeposited on Hg pool electrodes under the same conditions as in (a). Specific reflections expected for crystalline Ge with a diamond cubic lattice structure are indicated at the top. (c) Observed mean crystallite size (as determined through the line broadening in the powder X-ray diffractograms) in as-prepared Ge as a function of the applied potential used for electrodeposition at Hg pool electrodes. The dashed line indicates the least negative potential that facilitated Ge filament formation.

at more negative potentials. The diffraction patterns in Figure 2b indicated that the average crystalline domain size ranged between 53 and 8 nm for Ge electrodeposited between −1.2 and −2.7 V. The dependence was nonmonotonic, with a large decrease in average crystalline domain size between −1.2 and −1.9 V and a crystalline domain size of ∼8 nm between −1.9 and −2.7 V (Figure 2c).

Representative scanning electron microscopy (SEM) images of Ge electrodeposited at $E = -1.2$, −1.5, and −1.8 V are shown in Figure 3a−c. At $E = -1.2$ V, the deposit exhibited an irregular, particulate film morphology without any discernible arrangement. At more negative applied potentials, the grains thinned and appeared to be loosely interconnected. At $E = -1.8$ V, the as-deposited Ge films showed a dense leaflike structure. The texture of the Ge films changed markedly at potentials more negative than −1.9 V. Figure 3d shows three-dimensional (3D) mats of vertically aligned Ge filaments observed for films prepared at $E = -2.7$ V. The Figure 3d inset highlights the individual filament tips at the bottom of each film section. Bundles of filaments with footprints as large as 2.5×10^3 μm^2 were routinely observed,

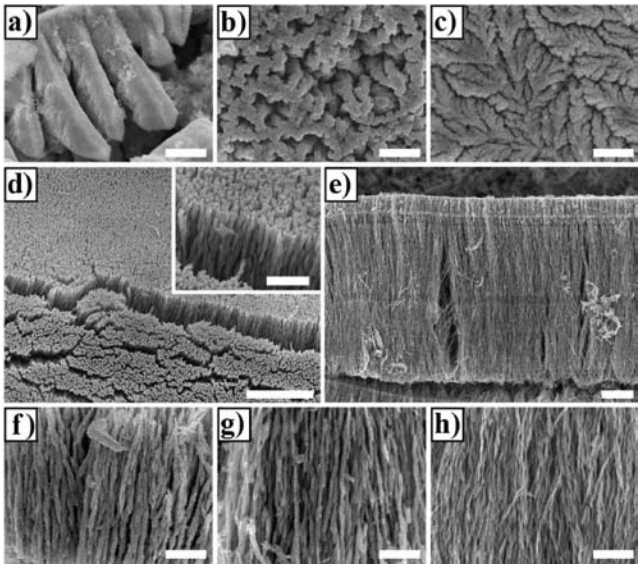

Figure 3. SEM micrographs of as-prepared Ge electrodeposited from the same electrolyte as in Figure 1 under various constant applied biases (E): (a) −1.2 V; (b) −1.5 V; (c) −1.8 V; (d) −2.7 V (the inset shows a higher-magnification view of the underside of a filament film section); (e) −2.7 V; (f) −2.1 V; (g) −2.4 V; (h) −2.7 V. Scale bars: (a−c) 0.5 μm; (d, e) 2 μm; (f−h) 0.5 μm.

indicating uniform morphology across the entire electrode surface area. The length of the dense mat of filaments depended on the total time of electrodeposition and was $\sim 10^{-5}$ m for long ($t \geq 2.5$ h) electrodeposition times. Figure 3e presents a side view showing the high density, uniformity, and length of the Ge filaments. The average diameter of the as-collected Ge filaments in Figure 3f-h was a function of the bias used for electrodeposition, with average diameters of 53 ± 16, 45 ± 14, and 26 ± 9 nm, respectively. Figure 3f−h also shows that the surfaces of the Ge filaments possessed a nodular texture with diameters that fluctuated slightly along their entire lengths.

The bright-field transmission electron microscopy (TEM) image of a representative Ge filament prepared via electrodeposition at $E = -2.7$ V (Figure 4a) shows the local fluctuation in the diameter of a filament. TEM micrographs also showed variations in the local contrast of individual filaments, indicating multiple and distinct crystalline domains. Phase-contrast TEM exhibited lattice fringes from multiple nonaligned crystallites as well as moiré fringes indicating partially misoriented crystalline domains with the same lattice parameter through the projected volume of the filaments (Figure S5). The selected-area electron diffraction (SAED) pattern collected for the same isolated filament (Figure 4b) confirmed the polycrystalline nature of the Ge filament and indicated a local structure consisting of multiple nonaligned domains of crystalline Ge. Figure 4c−e shows dark-field diffraction-contrast TEM micrographs collected using three distinct (220)-diffracted electron beams. In each of these dark-field images, the bright sections identify local regions within the filament at an orientation commensurate with the particular (220)-diffracted beam selected. The absence of any regular or consistent pattern in the contrast of the filaments across Figure 4c−e shows the absence of long-range ordering and preferred orientation of the Ge crystalline domains along the filament length, indicating that each Ge filament is a collection of randomly fused Ge crystallites. The electrical properties of the Ge filaments were assessed through single-filament

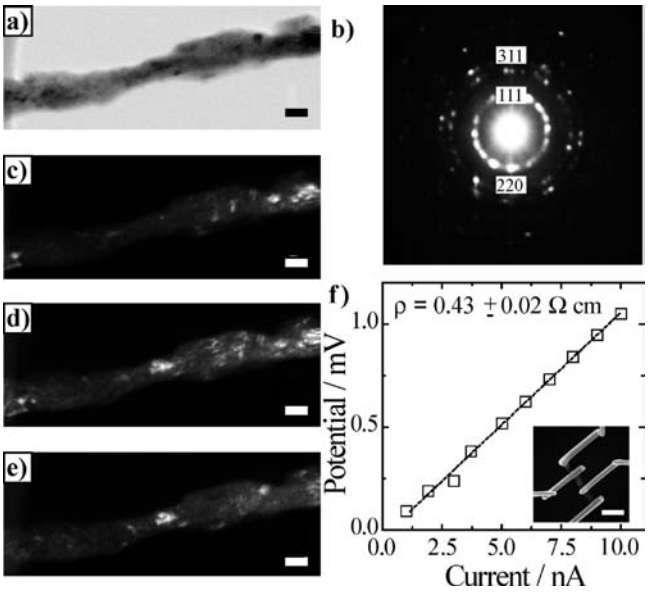

Figure 4. (a) Bright-field TEM micrograph of an individual Ge filament prepared via electrodeposition at $E = -2.7$ V in the same electrolyte as in Figure 1. (b) SAED pattern for the filament in (a). (c–e) Dark-field diffraction-contrast TEM images collected with three distinct electron beams diffracted along the <220> direction. (f) Voltage–current response for a single Ge filament device. The inset shows an electron micrograph of a Ge filament with four patterned metal contacts. Scale bars: (a, c–e) 20 nm; (f) 500 nm.

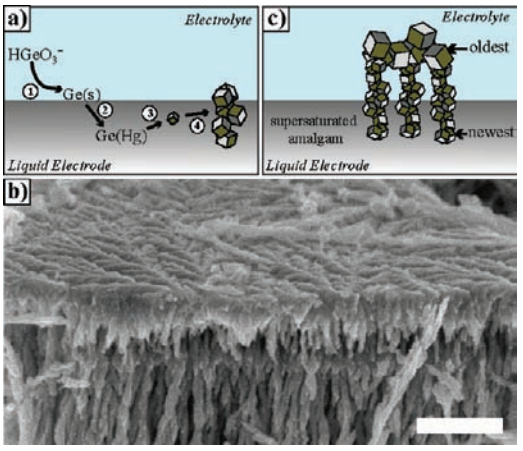

Figure 5. (a) Proposed description of the formation of crystalline Ge at Hg electrodes by ec-LLS: (1) $HGeO_3^-$(aq) is reduced at the Hg electrode surface; (2) Ge is dissolved into the Hg electrode; (3) the resultant Ge–Hg amalgam reaches the saturation point (dictated by the solubility of Ge in Hg and the flux of Ge into Hg), after which Ge crystallites (denoted as cubes) precipitate within the Hg pool; (4) the initial Ge crystallites serve as subsequent crystallization centers that produce polycrystalline aggregates. (b) SEM micrograph of an angled view of the top of a Ge filament film section (scale bar: 500 nm). (c) Proposed scheme for Ge filament growth. An initial dense layer of larger Ge particles provides nucleation points for unidirectional spherulitic filament growth. New extensions to the filament length occur within the Ge–Hg amalgam at the bottom of the film.

devices prepared via electron-beam patterning.[11] Contact resistances between Ge and Pt were nominally 10^7 Ω. The measured resistivities of the as-prepared Ge filaments were on the order of 0.4 Ω cm (Figure 4f),[12] which is much lower than expected for either amorphous Ge or undoped crystalline Ge.[13,14] Trace incorporation of Hg (a p-type dopant in Ge) is a likely contributor to the relatively low resistivity (Figure S6). Gated current–potential measurements showed no field dependence of the measured resistivity for gate voltages of ±20 V, precluding the determination of n- or p-type character. The measured resistivities were higher than expected for degenerate doping of crystalline Ge, but grain boundary scattering along the filament length could increase the resistance through a filament.[15] The present analyses do not rule out the possibility of degenerate doping under these conditions but do show that the as-prepared materials are of sufficient quality for electrical applications.

The cumulative data describe a three-step process for Ge electrodeposition at Hg involving reduction of $HGeO_3^-$(aq) to Ge, dissolution of Ge into the bulk Hg pool as an amalgam, and supersaturation of the Ge amalgam resulting in the precipitation of crystalline Ge (Figure 5a). The low solubility [$(2 \pm 0.5) \times 10^{-7}$ M] and diffusivity [$(1.3 \pm 0.1) \times 10^{-5}$ cm^2 s^{-1}] of Ge in Hg[5] support the contention that under high-current densities for Ge reduction, rapid saturation of the near-surface region of the Hg pool with Ge is achieved. In effect, Ge ec-LLS has stronger parallels specifically to systems involving precipitation from supersaturated solutions, such as polymer blends,[16] dissolved inorganic minerals,[17] and supercooled molten metal alloys,[18] rather than conventional electrodeposition at solid electrodes. For example, electrodeposition of ramified metal filaments (Figure S6)[19−21] is characterized by the presence of a strong electric field (10^1–10^3 V cm^{-1}) between two closely spaced electrodes,[21] a strong influence of the counterions on the electrolyte morphology and growth rate,[22] the formation of filament networks in a 2D plane,[20,21] and the lengthening of a metal filament via reduction of metal cations at the tip of an existing filament.[19,22] For electrodeposition of Ge filaments at Hg, the applied electric field between the working and counter electrodes was small (<1 V cm^{-1}); moreover, a change in the identity of the buffer electrolyte did not produce any perceptible change in the electrodeposition process or product, and the filaments formed extended 3D mats that covered the entire surface of the Hg pool with a thickness dictated by the electrodeposition time. SEM (Figure 5b) indicated that the tops of the Ge filament films had leaflike morphologies similar to that shown in Figure 3c and that discrete thin filaments emanate from the underside of this top layer. These aspects suggest that Ge filaments are produced through the formation of an initial dense layer of crystalline Ge followed first by rapid nucleation/precipitation of Ge in the supersaturated amalgam and then unidirectional spherulitic filament growth (i.e., dense polycrystalline filament growth from a plane rather than a central point) (Figure 5c). Spherulitic growth of filaments can occur in supersaturated solutions when the rotational and translational motion of nuclei during crystal formation are independent and prevent crystallization along a specific lattice direction.[23] Spherulitic filament growth in saturated mixtures requires a large gradient in the chemical potential of a precipitate (typically effected through temperature) to drive nucleation and directional solidification.[24] The depth-dependent Ge concentration within the liquid electrode, which is set by the rate of dissolution of Ge at the electrode–electrolyte interface, produces a chemical potential gradient for Ge in the amalgam. Although unidirectional spherulitic growth is not common,[24] the observed morphology and randomized orientation of the crystalline domains within the filaments are consistent with the predictions of spherulitic models.

The presented ec-LLS process for Ge preparation has several salient features. First, this electrodeposition scheme is a single-step benchtop process that is inherently less time- and energy-intensive than the standard routes for producing bulk quantities of crystalline Ge. The conventional industrial method for preparing crystalline Ge involves a multistep thermal reduction of GeO_2 (energy input $\gg$500 kJ mol^{-1}).[25−28] The energy input required to drive reaction 1 is only ∼270 kJ mol^{-1} at an overpotential of 0.6 V and a faradaic efficiency of 85%. Coupling Ge electrodeposition with a useful anodic half-reaction (e.g., anodic Cl_2 evolution) could yield an electrolysis process for producing valuable chemical/material products at both electrodes. Second, ec-LLS represents a new and controllable experimental design for studying polycrystalline nucleation from saturated mixtures. The ability to regulate precisely the conditions governing the flux of the soluble species into the liquid solvent (i.e., Hg) affords control and tunability that are not readily achievable in saturation/precipitation systems of general interest such as polymer blend crystallization,[16] gelation,[29] and mineral formation.[17] ec-LLS could prove useful for testing and validating evolving models of crystal nucleation.[30,31] Third, ec-LLS does not utilize any templating agent to produce various nanostructured morphologies. The filaments shown herein were free of residual organics and did not have to be removed from a porous template prior to electrical device incorporation, aspects that are atypical of wet-chemical syntheses of nanostructured semiconductors.[32,33] Furthermore, the conditions used for supersaturation/precipitation allow a myriad of distinct crystalline morphologies.[17] Fourth, ec-LLS is a general process. Although the data shown here are results specifically for Hg as the electrode material, we have performed analogous Ge electrodeposition experiments with liquid Ga electrodes and obtained similarly high levels of crystallinity. Differences in the physicochemical (e.g., surface tension, density) and electrochemical (i.e., electrocatalysis) properties of distinct liquid metal electrodes could substantially affect the morphology of the electrodeposited material and are currently under investigation. Initial results with Ga pool electrodes showed alternative morphologies of high-aspect-ratio Ge filaments. Other metals with low melting temperatures could also be envisioned as possible liquid electrodes under moderate (T < 300 °C) conditions. To date, such metal electrodes have not been ardently investigated specifically for semiconductor electrodeposition. This report provides new impetus for such work.

■ ASSOCIATED CONTENT

Supporting Information. Experimental methods; electrochemical data characterizing H_2 evolution and Ge electrodeposition at Hg, Cd, and Zn electrodes; Raman spectra of electrodeposits obtained at Cd and Zn; FTIR spectra, powder X-ray diffractograms, and high-resolution TEM images of Ge electrodeposited at Hg; a scheme depicting the mechanism of ramified metal filament electrodeposition. This material is available free of charge via the Internet at http://pubs.acs.org.

■ AUTHOR INFORMATION

Corresponding Author
smald@umich.edu

■ ACKNOWLEDGMENT

The authors gratefully acknowledge generous startup funds from the University of Michigan. The FEI Nova Nanolab Dual-Beam FIB-SEM, JEOL 3011 TEM, and JEOL 2010F (S)TEM instruments used in this work are maintained by the University of Michigan Electron Microbeam Analysis Laboratory through NSF support (DMR-0320740, DMR-0315633, and DMR-9871177, respectively). J.M.F. acknowledges a Rackham Merit Fellowship from the University of Michigan.

■ REFERENCES

(1) Williams, E. D.; Ayres, R. U.; Heller, M. *Environ. Sci. Technol.* **2002**, *36*, 5504.
(2) Liang, X.; Zhang, Q.; Lay, M. D.; Stickney, J. L. *J. Am. Chem. Soc.* **2011**, *133*, 8199.
(3) Hall, J. I.; Koenig, A. E. *Trans. Electrochem. Soc.* **1934**, *65*, 215.
(4) Fink, C. G.; Dokras, V. M. *J. Electrochem. Soc.* **1949**, *95*, 80.
(5) Karpiński, Z. J.; Kublik, Z. *J. Electroanal. Chem.* **1977**, *81*, 53.
(6) Karpiński, Z. J.; Połosak, A.; Kublik, Z. *Anal. Chim. Acta* **1980**, *120*, 55.
(7) Parker, J. H.; Feldman, D. W.; Ashkin, M. *Phys. Rev.* **1967**, *155*, 712.
(8) Wihl, M.; Cardona, M.; Tauc, J. *J. Non-Cryst. Solids* **1972**, *8−10*, 172.
(9) Fuji, M.; Hayashi, S.; Yamamoto, K. *Jpn. J. Appl. Phys.* **1991**, 30.
(10) Maeda, Y.; Tsukamoto, N.; Yazawa, Y.; Kanemitsu, Y.; Masumoto, Y. *Appl. Phys. Lett.* **1991**, *59*, 3168.
(11) Hanrath, T.; Korgel, B. A. *Proc. Inst. Mech. Eng., Part N* **2004**, *218*, 25.
(12) Walton, A. S.; Allen, C. S.; Critchley, K.; Górzny, M. Ł.; McKendry, J. E.; Brydson, R. M. D.; Hickey, B. J.; Evans, S. D. *Nanotechnology* **2007**, *18*, No. 065204.
(13) Walley, P. A. *Thin Solid Films* **1968**, *2*, 327.
(14) Hung, C. S.; Gliessman, J. R. *Phys. Rev.* **1954**, *96*, 1226.
(15) Baccarani, G.; Riccò, B.; Spadini, G. *J. Appl. Phys.* **1978**, *49*, 5565.
(16) Magill, J. H. *J. Mater. Sci.* **2001**, *36*, 3143.
(17) Beck, R.; Andreassen, J.-P. *Cryst. Growth Des.* **2010**, *10*, 2934.
(18) Li, D.; Herlach, D. M. *Phys. Rev. Lett.* **1996**, *77*, 1801.
(19) Chazalviel, J.-N. *Phys. Rev. A* **1990**, *42*, 7355.
(20) Fleury, V.; Kaufman, J. H.; Hibbert, D. B. *Nature* **1994**, *367*, 435.
(21) Fleury, V.; Rosso, M.; Chazalviel, J.-N.; Sapoval, B. *Phys. Rev. A* **1991**, *44*, 6693.
(22) Bazant, M. Z. *Phys. Rev. E* **1995**, *52*, 1903.
(23) Gránásy, L.; Pusztai, T.; Tegze, G.; Warren, J. A.; Douglas, J. F. *Phys. Rev. E* **2005**, *72*, No. 011605.
(24) Lovinger, A. J. *J. Appl. Phys.* **1978**, *49*, 5003.
(25) Adams, J. H. In *ASM Handbook*, 10th ed.; ASM International: Materials Park, OH, 1990; Vol. 2, p 733.
(26) Andon, R. J. L.; Mills, K. C. *J. Chem. Thermodyn.* **1971**, *3*, 583.
(27) Sommelet, P.; Orr, R. L. *J. Chem. Eng. Data* **1966**, *11*, 64.
(28) As noted in ref 25, preparation of polycrystalline Ge from GeO_2 requires thermal reduction of GeO_2 by H_2 at 760 °C followed by subsequent zone refining of the resultant Ge at 1000 °C. A lower bound for the energy input required by this process was calculated by considering the energy required to heat GeO_2 to 760 °C and then further heat the Ge to 1000 °C on the basis of the heat capacities presented in refs 25 and 26.
(29) Kumar, S. K.; Douglas, J. F. *Phys. Rev. Lett.* **2001**, *87*, No. 188301.
(30) Gránásy, L.; Pusztai, T.; Börzsönyi, T.; Warren, J. A.; Douglas, J. F. *Nat. Mater.* **2004**, *3*, 645.
(31) Kawasaki, T.; Tanaka, H. *Proc. Natl. Acad. Sci. U.S.A.* **2010**, *107*, 14036.
(32) Trindade, T.; O'Brien, P.; Pickett, N. L. *Chem. Mater.* **2001**, *13*, 3843.
(33) Trentler, T. J.; Hickman, K. M.; Goel, S. C.; Viano, A. M.; Gibbons, P. C.; Buhro, W. E. *Science* **1995**, *270*, 1791.